

Multi-level Asymmetric Contrastive Learning for Medical Image Segmentation Pre-training

Shuang Zeng

September 22, 2023

Abstract

Contrastive learning, which is a powerful technique for learning image-level representations from unlabeled data, leads a promising direction to dealing with the dilemma between large-scale pre-training and limited labeled data. However, most existing contrastive learning strategies are designed mainly for downstream tasks of natural images, therefore they are sub-optimal and even worse than learning from scratch when directly applied to medical images whose downstream tasks are usually segmentation. In this work, we propose a novel asymmetric contrastive learning framework named **JCL** for medical image segmentation with self-supervised pre-training. Specifically, (1) A novel asymmetric contrastive learning strategy is proposed to pre-train both encoder and decoder simultaneously in one-stage to provide better initialization for segmentation models. (2) A multi-level contrastive loss is designed to take the correspondence among feature-level, image-level and pixel-level projections, respectively into account to make sure multi-level representations can be learned by the encoder and decoder during pre-training. (3) Experiments on multiple medical image datasets indicate our JCL framework outperforms existing SOTA contrastive learning strategies.

1 Introduction

Medical image segmentation, defined as the partition of the entire image into different tissues, organs or other biologically relevant structures, plays a critical role in the computer-aided diagnosis paradigm which offers numerous benefits for clinical use. Although well pre-trained models can dramatically improve the performance of downstream segmentation task (e.g. MAE [15]), it is really a challenge to assemble such large annotated medical image datasets due to the extensive and burdensome annotation effort and the requirement of expertise. At the same time, a huge amount of unlabeled image data from modalities such as Computed Tomography (CT) and Magnetic Resonance Imaging (MRI) are generated every day all around the world. Therefore, it is highly desirable to propose some methods which can alleviate the following requirement: leverage numerous unlabeled data to pre-train models and achieve high performance with limited annotations.

Self-supervised learning (SSL) leads a promising direction to this dilemma: it provides a pre-training strategy that relies only on unlabeled data to obtain a suitable initialization for training downstream tasks with limited annotations. In recent years, SSL methods [11, 20, 12] have been highly successful for downstream analysis of not only natural images, but also medical images [37, 2, 33]. As a particular variant of SSL, contrastive learning (CL) [9, 16, 19] has shown great success in learning image-level features from large-scale unlabeled data which greatly reduces annotation costs. In CL framework setting, an encoder is initially pre-trained on unlabeled data to extract valuable image representations. Subsequently, the pre-trained encoder can serve as a well-suited initialization for training supervised downstream tasks, such as classification, object detection and image segmentation, which can be fine-tuned into an accurate model with additional modules (*e.g.* a projection head for classification or a decoder for segmentation), even with limited labeled data. In addition, CL framework also needs a suitable *contrastive loss* [9, 14] to pull the representations of similar pairs (*a.k.a.* positive pairs) together and push the representations of dissimilar pairs (*a.k.a.* negative pairs) apart, based on the fact that different augmentations of an image should have similar representations and those representations from different images should be dissimilar.

Despite its success, there are still some important issues to be solved when directly applying CL to medical image processing. On the one hand, most existing CL frameworks [32, 27] only pre-train

a single encoder, ignoring the characteristics of the downstream tasks in medical image processing, which are usually dense prediction tasks and require an additional decoder structure. Hence, the decoder is only trained from scratch during downstream fine-tuning. On the other hand, most works [16, 9, 13, 10] focus on extracting image-level projection and do not explicitly learn feature-level and pixel-level projections. These pre-trained models can be sub-optimal for dense prediction tasks due to the discrepancy between image-level projection and pixel-level projection and the missing of the implicit feature-level consistency.

In our work, a JCL framework is proposed to alleviate the above problems in the context of medical image processing. In order to get better initialization for the entire downstream segmentation model, the proposed JCL adopts a novel asymmetric CL strategy, which introduces a decoder into the one-stage CL framework and pre-trains the encoder and decoder simultaneously. In addition, a multi-level contrastive (MLC) loss is designed to take the correspondence among image-level, pixel-level and feature-level projections respectively into account to make sure multi-level representations can be learned by the encoder and decoder during pre-training.

2 Related Works

The core idea of CL is to attract the positive sample pairs and repulse the negative sample pairs through optimizing a model with InfoNCE [22] loss. In practice, CL methods benefit from a large number of negative samples [24, 28, 16, 9]. MoCo [16] introduces a dynamic memory bank to maintain a queue of negative samples. SimCLR [9] employs a substantial batch size to facilitate the coexistence of a significant number of negative samples within the current batch. Beyond the aforementioned classic training framework, SwAV [5] incorporates online clustering into Siamese network and proposes a new 'multi-crop' augmentation strategy that mixes the views of different resolutions. BYOL [13] introduces a slow-moving average network and shows that CL can be effective without any negative samples. By introducing stop-gradient, SimSiam [10] shows that simple Siamese networks can learn meaningful representations even without negative pairs, large batches or momentum encoders.

In the medical imaging domain, substantial efforts [3, 4, 8, 18, 31] have been devoted to incorporating unlabeled data to improve network performance due to the limited 3D data and annotations. As for CL, SimTriplet [17] proposes a *triplet-shape* CL framework which maximizes both intra-sample and inter-sample similarities via triplets from positive pairs without using negative samples to take advantage of multi-view nature of medical images. GCL [6] proposes a *partition-based* contrasting strategy which leverages structural similarity across volumetric medical images to divide unlabeled samples into positive and negative pairs and formulates a local version of contrastive loss to learn distinctive local representation used for per-pixel segmentation. PCL [32] further proposes a *position-based* CL framework to generate contrastive data pairs by leveraging the position information in volumetric medical images which can alleviate the problem that simple CL methods and GCL still introduce a lot of false negative pairs and result in degraded segmentation quality due to the circumstance where different medical images may have similar structures or organs.

3 Methods

This section first defines how to pre-train a model with CL for medical image segmentation. Then we propose a novel asymmetric framework which can pre-train both encoder and decoder in a single stage. Finally, the loss function design of JCL is discussed in Section 3.3 to consider multi-level representations.

3.1 Problem Definition

Given an input image $\mathbf{X} \in \mathbb{R}^{1 \times H \times W}$, medical image segmentation aims at classifying pixels in the image with a segmentation network, where $H \times W$ is the resolution of the image. To achieve this purpose, the segmentation network needs an encoder $e(\cdot)$ to extract multi-level features, and then a feature decoder $d(\cdot)$ is used to fuse the features into $\mathbf{Z} \in \mathbb{R}^{C \times H \times W}$ (C denotes channels) to recover image details:

$$\mathbf{Z} = d(\{\mathbf{X}^1, \mathbf{X}^2, \mathbf{X}^3, \mathbf{X}^4\}) = d(e(\mathbf{X})) \quad (1)$$

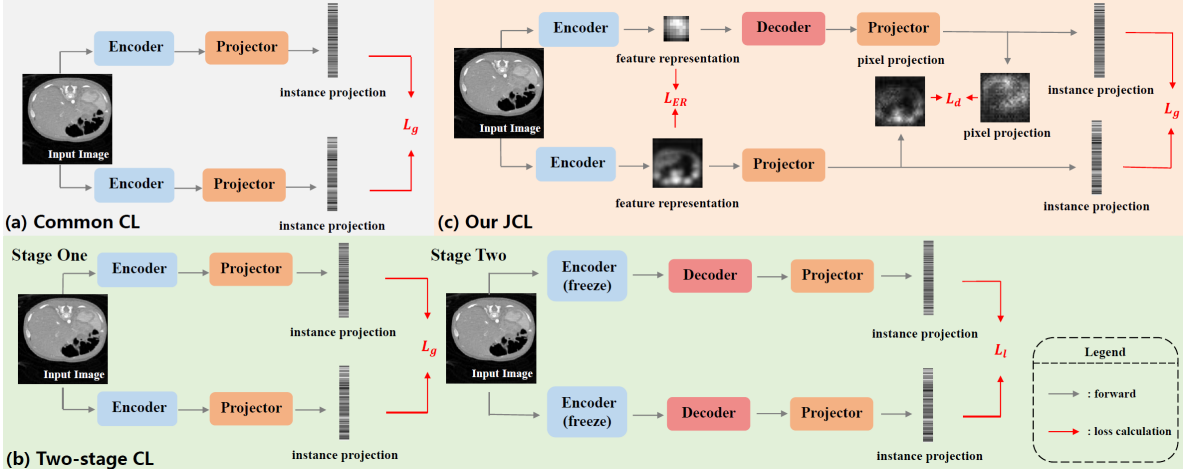


Figure 1: Comparison of different CL (contrastive learning) frameworks for medical images: (a) Common CL frameworks used for medical image segmentation are symmetrical and similar to SimCLR used for natural image. (b) Two-stage CL framework pre-trains the encoder with global contrastive loss and decoder with local contrastive loss in separate stage which ignores the collaboration between the encoder and decoder when pre-trained simultaneously. (c) Our proposed JCL framework is asymmetric with an additional decoder for pre-training and integrates multi-level contrastive loss including feature-level equivariant regularization, image-level and pixel-level contrastive loss to get better initialization of both encoder and decoder for downstream dense prediction tasks.

where \mathbf{X}^i represents the i_{th} -level feature. $e(\cdot)$ and $d(\cdot)$ are two hypothetic function that can be approximated by the network with learning parameter θ_e and θ_d . This fused feature \mathbf{Z} is finally classified by a segmentation head to output segmentation map.

Except for optimizing $e(\cdot)$ and $d(\cdot)$ from scratch, SSL focuses on pre-training them with numerous unlabeled data to provide suitable initialization before supervised learning for downstream segmentation task. However, as shown in Figure 1(a), most existing CL frameworks [6, 30] used for medical image segmentation are symmetrical and similar to SimCLR [9] used for natural images, which only pre-train an encoder $e(\cdot)$ with a global contrastive loss \mathcal{L}_g among image-level sample pairs.

$$\arg \min_{\theta_e} \mathcal{L}_g(e(\tilde{\mathbf{X}}), e(\hat{\mathbf{X}})) \quad (2)$$

where $\tilde{\mathbf{X}}$ and $\hat{\mathbf{X}}$ are two random augmentations of the input image \mathbf{X} . Apparently, the decoder structure $d(\cdot)$ is not considered in the above pre-training process, which ignores the importance of decoders [7, 34] to the downstream segmentation task. To solve this problem, as shown in Figure 1(b), GCL[6] proposes a two-stage CL framework which utilizes two pre-training stages to optimize $e(\cdot)$ with a global contrastive loss \mathcal{L}_g and $d(\cdot)$ with a local contrastive loss \mathcal{L}_l respectively:

$$\begin{cases} \arg \min_{\theta_e} \mathcal{L}_g(e(\tilde{\mathbf{X}}), e(\hat{\mathbf{X}})), & \text{in stage one} \\ \arg \min_{\theta_d} \mathcal{L}_l(d(e(\tilde{\mathbf{X}})), d(e(\hat{\mathbf{X}}))), & \text{in stage two} \end{cases} \quad (3)$$

where $\tilde{\mathbf{X}}$ and $\hat{\mathbf{X}}$ are two random augmentations of the input image \mathbf{X} , the parameters of $e(\cdot)$ are frozen in stage two. Although this strategy takes the decoder $d(\cdot)$ into consideration, the two-stage training process ignores the collaboration between the encoder and decoder during pre-training, which makes the decoder not able to learn image-level representation well due to the absence of global contrastive loss.

Based on the above issues, in order to realize the synchronous training of $e(\cdot)$ and $d(\cdot)$ to learn multi-level representations, we propose a novel one-stage multi-level asymmetric CL framework named JCL shown in Figure 1(c). Our JCL framework pre-trains the encoder $e(\cdot)$ and decoder $d(\cdot)$ simultaneously with both image-level global contrastive loss \mathcal{L}_g and pixel-level dense contrastive loss \mathcal{L}_d to learn multi-level feature representations:

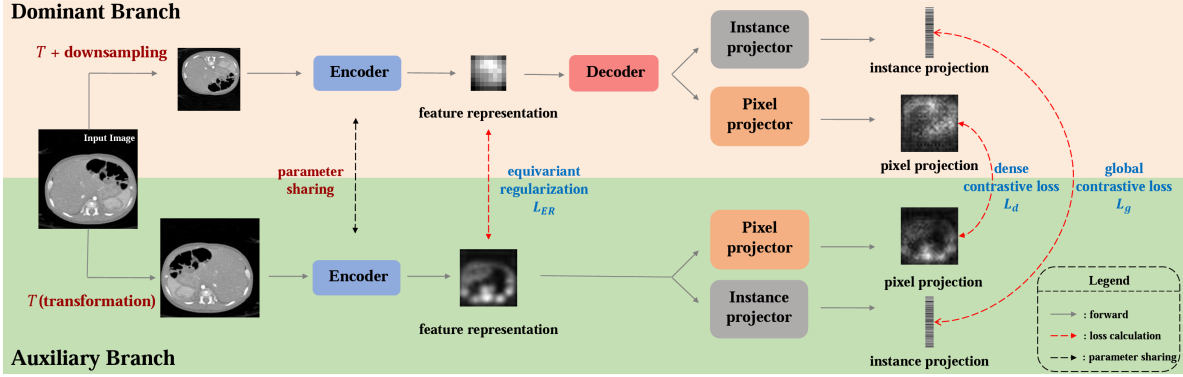


Figure 2: Overview of our proposed JCL (U-shape network but with only one partial decoder of single branch, like J-shape) framework. The input image is propagated to two branches: the dominant branch and auxiliary branch. In the dominant branch, after augmentation and downsampling, the input image is fitted into the encoder to get feature-level representation, and then propagated to the decoder and projector (including an instance projector and pixel projector) to get image-level and pixel-level projections; while in the auxiliary branch, only the same random augmentations are applied to the input (downsampling will be applied to the feature-level representation to guarantee feature alignment) and no decoder will be used. The feature-level representations from two branches will be used in equivariant regularization loss, and image-level and pixel-level projections will be used in global and dense contrastive loss respectively to achieve multi-level representations learning.

$$\arg \min_{\theta_e, \theta_d} \mathcal{L}_g(d(e(\tilde{\mathbf{X}})), d(e(\hat{\mathbf{X}}))) + \mathcal{L}_d(d(e(\tilde{\mathbf{X}})), d(e(\hat{\mathbf{X}}))) \quad (4)$$

where $\tilde{\mathbf{X}}$ and $\hat{\mathbf{X}}$ are two random augmentations of the input image \mathbf{X} . Our proposed JCL framework adopts an asymmetric CL strategy which pre-trains the encoder and decoder simultaneously in one-stage with a multi-level contrastive loss. So both the encoder and decoder can synchronously learn multi-level representations and get better initialization.

3.2 JCL Framework

In order to realize the one-stage synchronous training of encoder $e(\cdot)$ and decoder $d(\cdot)$ for better assisting the downstream dense prediction tasks, our JCL elaborates an asymmetric framework as shown in Figure 2. This proposed framework contains two branches: (1) *dominant branch* which pre-trains both encoder and decoder simultaneously to get better initialization for downstream dense prediction tasks and (2) *auxiliary branch* which serves as a contrastive counterpart to assist the dominant branch for pre-training.

The auxiliary branch keeps in line with that of common CL strategies: an encoder $e(\cdot)$ followed by a shallow multi-layer perceptron (MLP) projection head $\tilde{g}(\cdot)$ [9] (but including an image-level projector $\tilde{g}_{ins}(\cdot)$ and pixel-level projector $\tilde{g}_{pix}(\cdot)$) and no decoder. Specifically, random augmentations $aug(\cdot)$ are applied to the input image \mathbf{X} , and then the augmented image is propagated to the encoder $e(\cdot)$ to get feature-level representation $\tilde{\mathbf{Y}}$:

$$\tilde{\mathbf{Y}} = e((aug(\mathbf{X}))) \quad (5)$$

Then $\tilde{\mathbf{Y}}$ is propagated into the image-level projector $\tilde{g}_{ins}(\cdot)$ and pixel-level projector $\tilde{g}_{pix}(\cdot)$ to get image-level projection $\tilde{\mathbf{Z}}^g \in \mathbb{R}^{B \times C}$ (where B denotes batch size, C denotes channels) and pixel-level projection $\tilde{\mathbf{Z}}^l \in \mathbb{R}^{B \times C \times H \times W}$ (where B denotes batch size, C denotes channels, H denotes image height, W denotes image width) respectively:

$$\begin{aligned} \tilde{\mathbf{Z}}^g &= \tilde{g}_{ins}(\tilde{\mathbf{Y}}) \\ \tilde{\mathbf{Z}}^l &= \tilde{g}_{pix}(\tilde{\mathbf{Y}}) \end{aligned} \quad (6)$$

Different from the auxiliary branch, the dominant branch introduces a decoder $d(\cdot)$ after the encoder $e(\cdot)$ for synchronous pre-training to dig more information from feature-level representation which is

beneficial to the downstream dense prediction tasks. The decoder $d(\cdot)$ is also followed by a MLP projection head $g(\cdot)$ (including an image-level projector $g_{ins}(\cdot)$ and pixel-level projector $g_{pix}(\cdot)$ as well). Specifically, the same augmentations are applied to the input image \mathbf{X} , moreover, due to the introduction of the decoder in this branch, the size of feature maps from two branches will be different if inputs are same. Hence, we add downsampling $down(\cdot)$ into data augmentation to align features which can also guarantee sufficient negative sample pairs due to its small computation complexity. The augmented image is then propagated to the encoder $e(\cdot)$ which shares the same parameters with that in the auxiliary branch to get the feature-level representation \mathbf{Y} :

$$\mathbf{Y} = e(down(aug(\mathbf{X}))) \quad (7)$$

Next, \mathbf{Y} will be propagated into the decoder $d(\cdot)$ to recover image details, and then propagated into the image-level projector $g_{ins}(\cdot)$ and pixel-level projector $g_{pix}(\cdot)$ to get image-level projection \mathbf{Z}^g and pixel-level projection \mathbf{Z}^l , respectively:

$$\begin{aligned} \mathbf{Z}^g &= g_{ins}(d(\mathbf{Y})) \\ \mathbf{Z}^l &= g_{pix}(d(\mathbf{Y})) \end{aligned} \quad (8)$$

With such a novel asymmetric network structure to guarantee the feature alignment between the representation output after $e(\cdot)$, $d(\cdot)$ in the dominant branch and that output after $e(\cdot)$ in the auxiliary branch, we can realize one-stage synchronous training of $e(\cdot)$ and $d(\cdot)$ with more negative sample pairs and less computation complexity for better assisting the downstream dense prediction tasks.

3.3 Multi-Level Contrastive Loss

Under the guarantee of our proposed asymmetric JCL framework in Section 3.2 which pre-trains the encoder and decoder simultaneously, our loss design can consider multi-level feature representations including image-level, pixel-level and feature-level representations in the meantime. We optimize the JCL framework with multi-level contrastive (MLC) loss \mathcal{L}_{MLC} as follows:

$$\mathcal{L}_{MLC} = \lambda_1 \mathcal{L}_g + \lambda_2 \mathcal{L}_d + \lambda_3 \mathcal{L}_{ER} \quad (9)$$

where $\lambda_1, \lambda_2, \lambda_3$ are the weighting factors, and the overall pre-training is conducted in one-stage manner. We give the details of network training settings and carefully investigate the effectiveness of each module in the experiments section.

3.3.1 Global Contrastive Loss

The image-level representation is regulated by the global contrastive loss. Specifically, for a set of N randomly sampled slices, $\{X_i\}_{i=1\dots N}$, the corresponding mini-batch consists of $2N$ samples after data augmentation, $\{\tilde{X}_i\}_{i=1\dots 2N}$, in which \tilde{X}_{2i} and \tilde{X}_{2i-1} are two random augmentations of X_i . Z_i^g, \tilde{Z}_i^g represent the learned image-level projection of \tilde{X}_i from the dominant branch and auxiliary branch, respectively. Then the global contrastive loss can be formulated as:

$$\mathcal{L}_g = \sum_{i=1}^{2N} -\frac{1}{|\Omega_i^+|} \sum_{j \in \Omega_i^+} \log \frac{e^{sim(Z_i^g, \tilde{Z}_j^g)/\tau}}{\sum_{k=1}^{2N} \mathbb{1}_{i \neq k} \cdot e^{sim(Z_i^g, \tilde{Z}_k^g)/\tau}} \quad (10)$$

where $|\Omega_i^+|$ is the set of indices of positive samples to \tilde{X}_i . $sim(\cdot, \cdot)$ is the cosine similarity function that computes the similarity between two vectors in the representation space. τ is a temperature scaling parameter. Compared with the standard contrastive loss [9] that only has one positive pair on the numerator for any sample X_i , we use the contrastive pair generation strategy in PCL [32] to form *position-based* positive and negative pairs. All positive pairs (*e.g.* the augmented one and any of the remaining $2(N-2)$ samples whose *position* is close to X_i) in a mini-batch in Eq.10 contribute to the numerator, allowing better utilization of the proposed strategy.

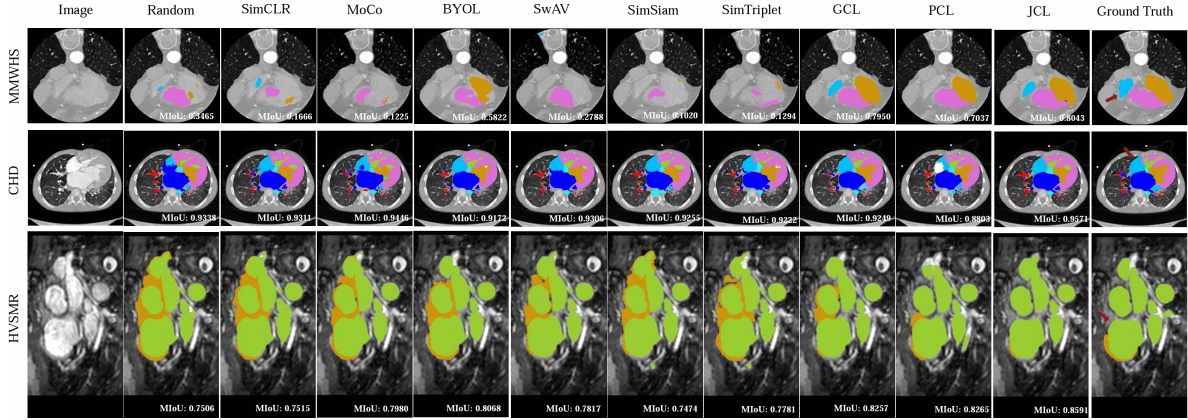


Figure 3: Visualization of segmentation results on all datasets. The results of MMWHS, CHD, and HVSMR are generated from the fine-tuned models of $[M=6, \text{fold}=1]$, $[M=10, \text{fold}=3]$ and $[M=6, \text{fold}=4]$, respectively. M is the number of patients used for fine-tuning.

3.3.2 Dense Contrastive Loss

The pixel-level representation is forced by a proposed dense contrastive loss which takes the correspondence between the pixel-level features into account and extends the original global contrastive loss to a dense paradigm. In detail, for a set of N randomly sampled slices, $\{X_i\}_{i=1\dots N}$, the corresponding mini-batch consists of $2N$ samples after data augmentation, $\{\tilde{X}_i\}_{i=1\dots 2N}$, in which \tilde{X}_{2i} and \tilde{X}_{2i-1} are two random augmentations of X_i . Different from the image-level projection Z_i^g and \tilde{Z}_i^g , Z_i^l and \tilde{Z}_i^l are pixel-level projections generated by the pixel-level projector in the dominant and auxiliary branch, respectively, which are dense feature maps with a size of $S \times S$. S denotes the spatial size of the generated dense feature maps. For every two input images, we can form S^2 pixel-level projection pairs (positive or negative pairs depending on Δ position) according to the *position-based* contrastive pair generation strategy. So the dense contrastive loss can be defined as:

$$\mathcal{L}_d = \sum_{i=1}^{2N} -\frac{1}{|\Omega_i^+|} \sum_{j \in \Omega_i^+} \frac{1}{S^2} \sum_s \log \frac{e^{\text{sim}(Z_{i,s}^l, \tilde{Z}_{j,s}^l)/\tau}}{\sum_{k=1}^{2N} \mathbb{1}_{i \neq k} \cdot e^{\text{sim}(Z_{i,s}^l, \tilde{Z}_{k,s}^l)/\tau}} \quad (11)$$

where $Z_{i,s}^l$ and $\tilde{Z}_{i,s}^l$ denote the s th output of S^2 pixel-level projection pairs of \tilde{X}_i from the dominant branch and auxiliary branch, respectively.

3.3.3 Equivariant Regularization

The feature-level representation is governed by equivariant regularization [26]. Specifically, due to the introduction of downsampling in the dominant branch, the feature representations from the two encoders are different in size, therefore, we incorporate equivariant regularization into our MLC loss to apply consistency regularization on multi-scale feature representations to provide further self-supervision for network learning. The equivariant regularization can be formulated as:

$$\mathcal{L}_{ER} = \|\mathbf{Y} - \text{down}(\tilde{\mathbf{Y}})\|_1 \quad (12)$$

where \mathbf{Y} and $\tilde{\mathbf{Y}}$ are the representations learned from the encoder in the dominant and auxiliary branch, respectively. We use L1 norm here to integrate consistency regularization on feature representations from the encoders to provide further self-supervision for network learning.

4 Experiments

In this section, the settings of experiments are first detailed. Then quantitative and qualitative results of our method are given for comparison with the state-of-the-art methods. Finally, the superiority and limitation of our JCL are further discussed to inspire future works. More experiments are also given in our Supplementary Materials.

4.1 Settings

Datasets: We evaluate the performance of the proposed JCL on three publicly available medical image datasets. **(1) The Congenital Heart Disease (CHD) dataset** is a CT dataset that consists of 68 3D cardiac images captured by a Simens biograph 64 machine [29]. The dataset covers 14 types of congenital heart disease and the segmentation labels include seven substructures: left ventricle (LV), right ventricle (RV), left atrium (LA), right atrium (RA), myocardium (Myo), aorta (Ao) and pulmonary artery (PA). **(2) Multi-Modality Whole Heart Segmentation (MMWHS) dataset** was hosted in STACOM and MICCAI 2017 [35, 36]. It consists of 20 cardiac CT and 20 MRI images and the annotations include the same seven substructures as the CHD dataset. And we use the 20 cardiac CT images for pre-training and fine-tuning. **(3) The High-Value Health Care Project for Structural Heart Disease MRI Segmentation (HVSMD) dataset** was hosted in MICCAI 2016 challenge [23]. It has 10 3D cardiac MRI images captured in an axial view on a 1.5T scanner. Manual annotations of blood pool and Myo are provided.

Pre-processing: Following the pipeline of GCL [6], we first normalize the intensity of each 3D volume x to $[x_1, x_{99}]$, where x_p is the p -th intensity percentile in x . Then all 2D slices and the corresponding annotations are resampled to a fixed spatial resolution f_r and padded to a fixed image size f_s with 0. We do not apply cropping because it may remove the important structure information in the original slice. The f_r and f_s for each dataset are defined as follows: (1) CHD dataset: $f_r = 1.0 \times 1.0mm^2$ and $f_s = 512 \times 512$, (2) MMWHS dataset: $f_r = 1.0 \times 1.0mm^2$ and $f_s = 256 \times 256$, (3) HVSMD dataset: $f_r = 0.7 \times 0.7mm^2$ and $f_s = 352 \times 352$. No additional alignment is used for CHD dataset because it is already roughly aligned when acquired.

Implementation Details: We employ our JCL framework to pre-train a U-Net encoder and two-block decoder on the whole CHD dataset without using any human label. Then the pre-trained model is used as the initialization to fine-tune a U-Net segmentation network (that is to say we add the remaining decoder blocks so that the output of the network has the same dimensions as the input) with a small number of labeled samples of CHD, MMWHS and HVSMD datasets, respectively. Details of network architectures are provided in Supplementary Materials. 5-fold cross-validation is used to evaluate the segmentation performance. Experiments of pre-training and fine-tuning are conducted on two NVidia A100 GPUs in DistributedData Parallel (DDP). Data augmentations, including translation, rotation and scale are used in both the pre-training and fine-tuning stage and downsampling with a scale factor of 0.25 is used only in the pre-training stage. In the pre-training stage, the threshold t is set to be 0.1 for CHD, the weighted terms $\{\lambda_1, \lambda_2, \lambda_3\}$ are set to be $\{1.0, 0.5, 1.0\}$, temperature τ is set to be 0.1, the model is trained with 100 epochs, 16 batches per GPU, SGD optimizer and initial learning rate of 0.1, which is then decayed with the cosine scheduler on each training iterator. In the fine-tuning stage, we train the U-Net with cross-entropy loss for 100 epochs with Adam optimizer. The batch size per GPU is set to be 5, and initial learning rate is $5 \times e^{-4}$ which is then decayed with cosine scheduler to minimum learning rate $5 \times e^{-6}$.

4.2 Results

In this section, we evaluate the performance of our proposed JCL from quantitative and qualitative perspectives on the above datasets. The visualization of more segmentation results are given in Supplementary Materials.

We compare the performance of our JCL with a random approach which does not use any pre-training as well as other state-of-the-art baselines, including SimCLR [9], MoCo [16], BYOL [13], SwAV [5], SimSiam [10] in natural imaging domain and SimTriplet [17], GCL [6], PCL [32] in medical imaging domain. All the experiments across different methods have the same dataset settings and partition, and all the methods have the same backbone structures. The quantitative results of the comparative study carried on CHD are shown in Table 1. We report the averaging Dice of 5-fold cross-validation results. From Table 1, we have the following observations. (1) In general, benefited from our proposed asymmetric CL framework which pre-trains encoder and decoder simultaneously together with multi-level contrastive (MLC) loss, our JCL outperforms all the existing SOTA baselines in almost all values of M except for $M = 51$, *i.e.* 0.10 Dice higher than SimSiam on average when $M = 6$ and 0.02 Dice higher than PCL on average when $M = 10$. (2) The performance improvement of our proposed JCL is high when a small number of training samples is used (e.g. $M = 6, 10$) and the gains become lesser when the number of training samples increases. This is because with more

Method	CHD (68 patients in total)				
	$M = 6$	$M = 10$	$M = 15$	$M = 20$	$M = 51$
Random	0.5198(.06)	0.6144(.04)	0.6575(.05)	0.6935(.04)	0.7686(.03)
SimCLR	0.5248(.05)	0.6149(.04)	0.6631(.04)	0.6914(.04)	0.7624(.03)
MoCo	0.5077(.05)	0.6064(.05)	0.6519(.04)	0.6867(.04)	0.7599(.02)
BYOL	0.5116(.06)	0.6235(.05)	0.6498(.05)	0.6863(.04)	0.7689(.03)
SwAV	0.5037(.07)	0.6188(.05)	0.6552(.05)	0.6946(.04)	0.7721(.03)
SimSiam	0.4669(.06)	0.5918(.04)	0.6391(.05)	0.6782(.04)	0.7606(.03)
SimTriplet	0.4987(.07)	0.6000(.04)	0.6365(.05)	0.6884(.03)	0.7605(.04)
GCL	0.5297(.06)	0.6368(.03)	0.6643(.05)	0.6928(.04)	0.7708(.03)
PCL	0.5243(.05)	0.6234(.04)	0.6672(.05)	0.6875(.05)	0.7673(.03)
JCL (Ours)	0.5620(.05)	0.6499(.03)	0.6754(.04)	0.7007(.04)	0.7622(.04)

Table 1: Comparison of our proposed JCL method with baseline methods on CHD. M is the number of patients used in the fine-tuning process. Results are reported in the form of mean (standard deviation) on the 5-fold cross-validation.

Method	CHD transferring to MMWHS (20 patients in total)				
	$M = 6$	$M = 8$	$M = 10$	$M = 12$	$M = 16$
Random	0.8224(.06)	0.8573(.03)	0.8769(.02)	0.8847(.02)	0.9004(.01)
SimCLR	0.8129(.06)	0.8620(.03)	0.8725(.02)	0.8850(.02)	0.8980(.01)
MoCo	0.8047(.06)	0.8491(.03)	0.8695(.03)	0.8821(.02)	0.8961(.01)
BYOL	0.8196(.05)	0.8629(.03)	0.8768(.02)	0.8881(.02)	0.8988(.01)
SwAV	0.8173(.06)	0.8491(.03)	0.8695(.03)	0.8821(.02)	0.8961(.01)
SimSiam	0.7970(.07)	0.8496(.04)	0.8643(.03)	0.8829(.02)	0.8955(.01)
SimTriplet	0.7994(.07)	0.8566(.03)	0.8654(.03)	0.8832(.02)	0.8947(.01)
GCL	0.8107(.07)	0.8569(.03)	0.8791(.02)	0.8866(.02)	0.9002(.01)
PCL	0.8467(.03)	0.8721(.03)	0.8832(.02)	0.8931(.02)	0.9019(.01)
JCL (Ours)	0.8517(.03)	0.8746(.03)	0.8871(.02)	0.8961(.01)	0.9034(.01)

Table 2: Transfer learning comparison of our proposed JCL method with the baselines. Except for Random, all the methods are pre-trained on CHD without labels and fine-tuned on MMWHS.

training samples, the information difference between the training dataset for fine-tuning and for CL pre-training becomes small and the fine-tuning performance saturates, which explains why our JCL is slightly inferior to other baselines when $M = 51$, and all the methods perform very closely.

We use the encoder and decoder in the dominant branch pre-trained on CT dataset CHD without labels as the initialization of a U-Net to fine-tune on MMWHS with the same modality CT to assess whether the learned representations by our JCL are transferrable. The experimental setup and baselines are the same as in semi-supervised learning. Table 2 shows the comparison results on MMWHS. It can be seen that our proposed JCL framework outperforms all baselines on MMWHS, *i.e.* 0.10 Dice higher than SimSiam on average when $M = 6$ and 0.03 Dice higher than GCL on average when $M = 8$ of MMWHS. The visualization of segmentation results on CHD and MMWHS is shown in Figure 3. It can be seen that compared with baseline CL methods, we can get the correct number of classes of substructures, *i.e.* BYOL and SimSiam only segment two classes of substructures with 0.5822 and 0.1020 mIoU, respectively on MMWHS while our JCL is 0.8043 mIoU. Compared with PCL and GCL, our JCL can get more precise regions of substructures with higher mIoU, *i.e.* our JCL outperforms 10.1% mIoU promotion on MMWHS compared with PCL, and 3.2% and 7.7% mIoU promotion on CHD compared with GCL and PCL.

4.3 Discussions

Ablation Studies: Ablation studies have been conducted to verify the effectiveness of each part of our proposed components, *e.g.* the decoder structure, equivariant regularization \mathcal{L}_{ER} and dense contrastive loss \mathcal{L}_d of our proposed JCL framework. Results are reported in Table 3. It can be seen that each part of our proposed components contributes to the improvement of performance. Specifically, the introduction of decoder structure and pixel-level dense contrastive loss \mathcal{L}_d improves

Framework	Settings				CHD		HVSMR	
	\mathcal{L}_g	decoder	\mathcal{L}_{ER}	\mathcal{L}_d	$M = 6$	$M = 15$	$M = 2$	$M = 8$
PCL	✓				0.5243(.05)	0.6672(.05)	0.7974(.03)	0.8493(.04)
PCL + decoder	✓	✓			0.5410(.05)	0.6708(.04)	0.8047(.04)	0.8525(.03)
JCL (image-level)	✓	✓	✓		0.5475(.05)	0.6753(.04)	0.8082(.04)	0.8574(.04)
JCL	✓	✓	✓	✓	0.5620(.05)	0.6754(.04)	0.8165(.03)	0.8604(.03)

Table 3: The ablation studies for each component of JCL.

CHD generalizing to HVSMR (10 patients in total)			
Method	$M = 2$	$M = 6$	$M = 8$
Random	0.7794(.06)	0.8483(.04)	0.8427(.05)
SimCLR	0.7692(.07)	0.8371(.04)	0.8432(.04)
MoCo	0.7537(.08)	0.8326(.05)	0.8331(.05)
BYOL	0.7826(.06)	0.8448(.03)	0.8410(.05)
SwAV	0.7669(.08)	0.8381(.04)	0.8422(.04)
SimSiam	0.7691(.06)	0.8229(.06)	0.8342(.06)
SimTriplet	0.7857(.04)	0.8286(.05)	0.8422(.04)
GCL	0.7714(.04)	0.8416(.04)	0.8457(.04)
PCL	0.7974(.03)	0.8520(.03)	0.8493(.04)
JCL (Ours)	0.8165(.03)	0.8533(.03)	0.8604(.03)

Table 4: Generalization to different modalities comparison of our proposed JCL method with the baselines.

the performance of our JCL framework to a greater extent compared with the slight promotion of equivariant regularization \mathcal{L}_{ER} , *i.e.* 0.017 and 0.015 Dice promotion when applying the decoder and \mathcal{L}_d respectively while 0.007 Dice promotion when applying \mathcal{L}_{ER} when $M = 6$ of CHD, verifying the effectiveness of our proposed asymmetric CL framework and multi-level contrastive (MLC) loss. Moreover, we have further conducted an ablation study on the number of blocks ($N = 0,1,2,3,4$) of the decoder, different connection modes (two parameter-shared, two independent encoders or encoder with EMA) to verify the best components combination. And We have also conducted experiments on variants of U-Net (including UCTransNet [25], Attention U-Net [21] and BCDUNet [1]) to verify generalization and universality of our proposed JCL. The experimental results of other ablations are shown in Supplementary Materials.

Generalization to Different Modalities: Besides fine-tuning our JCL on CHD for semi-supervised learning and the same modality CT dataset MMWHS for transfer learning, we have also conducted experiments to compare the performance of our JCL with these SOTA baselines to illustrate the generalization of our JCL on MRI dataset HVSMR. Table 4 shows the comparison results on HVSMR. It can be seen that our proposed JCL still outperforms all baselines on various M of HVMSR. The visualization results are also shown in Figure 3. SimSiam can only get 0.7474 mIoU which even performs worse than learning from scratch with 0.7506 mIoU, while the performance of our JCL is 0.8591 mIoU which is still much higher than the previous two best methods GCL and PCL with 0.8257 and 0.8265 mIoU.

5 Conclusion

In this work, we propose a novel asymmetric CL framework named JCL for medical image segmentation with self-supervised pre-training. Specifically, a novel asymmetric CL strategy is proposed to pre-train both encoder and decoder simultaneously in only one stage to provide better initialization for segmentation models during synchronous training. In addition, a multi-level contrastive (MLC) loss is designed to take the correspondence among feature-level, image-level and pixel-level projections, respectively into account to make sure multi-level representations can be learned by the encoder and decoder during pre-training. Experiments on multiple medical image datasets indicate our JCL framework outperforms existing SOTA CL strategies.

References

- [1] Reza Azad, Maryam Asadi-Aghbolaghi, Mahmood Fathy, and Sergio Escalera. Bi-directional convlstm u-net with densely connected convolutions. In *Proceedings of the IEEE/CVF international conference on computer vision workshops*, pages 0–0, 2019.
- [2] Wenjia Bai, Chen Chen, Giacomo Tarroni, Jinming Duan, Florian Guitton, Steffen E Petersen, Yike Guo, Paul M Matthews, and Daniel Rueckert. Self-supervised learning for cardiac mr image segmentation by anatomical position prediction. In *Medical Image Computing and Computer Assisted Intervention–MICCAI 2019: 22nd International Conference, Shenzhen, China, October 13–17, 2019, Proceedings, Part II 22*, pages 541–549. Springer, 2019.
- [3] Wenjia Bai, Chen Chen, Giacomo Tarroni, Jinming Duan, Florian Guitton, Steffen E Petersen, Yike Guo, Paul M Matthews, and Daniel Rueckert. Self-supervised learning for cardiac mr image segmentation by anatomical position prediction. In *Medical Image Computing and Computer Assisted Intervention–MICCAI 2019: 22nd International Conference, Shenzhen, China, October 13–17, 2019, Proceedings, Part II 22*, pages 541–549. Springer, 2019.
- [4] Gerda Bortsova, Florian Dubost, Laurens Hogeweg, Ioannis Katramados, and Marleen De Bruijne. Semi-supervised medical image segmentation via learning consistency under transformations. In *Medical Image Computing and Computer Assisted Intervention–MICCAI 2019: 22nd International Conference, Shenzhen, China, October 13–17, 2019, Proceedings, Part VI 22*, pages 810–818. Springer, 2019.
- [5] Mathilde Caron, Ishan Misra, Julien Mairal, Priya Goyal, Piotr Bojanowski, and Armand Joulin. Unsupervised learning of visual features by contrasting cluster assignments. *Advances in neural information processing systems*, 33:9912–9924, 2020.
- [6] Krishna Chaitanya, Ertunc Erdil, Neerav Karani, and Ender Konukoglu. Contrastive learning of global and local features for medical image segmentation with limited annotations. *Advances in Neural Information Processing Systems*, 33:12546–12558, 2020.
- [7] Liang-Chieh Chen, George Papandreou, Iasonas Kokkinos, Kevin Murphy, and Alan L Yuille. Deeplab: Semantic image segmentation with deep convolutional nets, atrous convolution, and fully connected crfs. *IEEE transactions on pattern analysis and machine intelligence*, 40(4):834–848, 2017.
- [8] Shuai Chen, Gerda Bortsova, Antonio García-Uceda Juárez, Gijs Van Tulder, and Marleen De Bruijne. Multi-task attention-based semi-supervised learning for medical image segmentation. In *Medical Image Computing and Computer Assisted Intervention–MICCAI 2019: 22nd International Conference, Shenzhen, China, October 13–17, 2019, Proceedings, Part III 22*, pages 457–465. Springer, 2019.
- [9] Ting Chen, Simon Kornblith, Mohammad Norouzi, and Geoffrey Hinton. A simple framework for contrastive learning of visual representations. In *International conference on machine learning*, pages 1597–1607. PMLR, 2020.
- [10] Xinlei Chen and Kaiming He. Exploring simple siamese representation learning. In *Proceedings of the IEEE/CVF conference on computer vision and pattern recognition*, pages 15750–15758, 2021.
- [11] Carl Doersch, Abhinav Gupta, and Alexei A Efros. Unsupervised visual representation learning by context prediction. In *Proceedings of the IEEE international conference on computer vision*, pages 1422–1430, 2015.
- [12] Spyros Gidaris, Praveer Singh, and Nikos Komodakis. Unsupervised representation learning by predicting image rotations. *arXiv preprint arXiv:1803.07728*, 2018.
- [13] Jean-Bastien Grill, Florian Strub, Florent Altché, Corentin Tallec, Pierre Richemond, Elena Buchatskaya, Carl Doersch, Bernardo Avila Pires, Zhaohan Guo, Mohammad Gheshlaghi Azar, et al. Bootstrap your own latent—a new approach to self-supervised learning. *Advances in neural information processing systems*, 33:21271–21284, 2020.

- [14] Raia Hadsell, Sumit Chopra, and Yann LeCun. Dimensionality reduction by learning an invariant mapping. In *2006 IEEE Computer Society Conference on Computer Vision and Pattern Recognition (CVPR'06)*, volume 2, pages 1735–1742. IEEE, 2006.
- [15] Kaiming He, Xinlei Chen, Saining Xie, Yanghao Li, Piotr Dollár, and Ross Girshick. Masked autoencoders are scalable vision learners. In *Proceedings of the IEEE/CVF Conference on Computer Vision and Pattern Recognition*, pages 16000–16009, 2022.
- [16] Kaiming He, Haoqi Fan, Yuxin Wu, Saining Xie, and Ross Girshick. Momentum contrast for unsupervised visual representation learning. In *Proceedings of the IEEE/CVF conference on computer vision and pattern recognition*, pages 9729–9738, 2020.
- [17] Quan Liu, Peter C Louis, Yuzhe Lu, Aadarsh Jha, Mengyang Zhao, Ruining Deng, Tianyuan Yao, Joseph T Roland, Haichun Yang, Shilin Zhao, et al. Simtriplet: Simple triplet representation learning with a single gpu. In *Medical Image Computing and Computer Assisted Intervention–MICCAI 2021: 24th International Conference, Strasbourg, France, September 27–October 1, 2021, Proceedings, Part II 24*, pages 102–112. Springer, 2021.
- [18] Xiangde Luo, Jieneng Chen, Tao Song, and Guotai Wang. Semi-supervised medical image segmentation through dual-task consistency. In *Proceedings of the AAAI Conference on Artificial Intelligence*, volume 35, pages 8801–8809, 2021.
- [19] Ishan Misra and Laurens van der Maaten. Self-supervised learning of pretext-invariant representations. In *Proceedings of the IEEE/CVF conference on computer vision and pattern recognition*, pages 6707–6717, 2020.
- [20] Mehdi Noroozi and Paolo Favaro. Unsupervised learning of visual representations by solving jigsaw puzzles. In *Computer Vision–ECCV 2016: 14th European Conference, Amsterdam, The Netherlands, October 11–14, 2016, Proceedings, Part VI*, pages 69–84. Springer, 2016.
- [21] Ozan Oktay, Jo Schlemper, Loic Le Folgoc, Matthew Lee, Mattias Heinrich, Kazunari Misawa, Kensaku Mori, Steven McDonagh, Nils Y Hammerla, Bernhard Kainz, et al. Attention u-net: Learning where to look for the pancreas. *arXiv preprint arXiv:1804.03999*, 2018.
- [22] Aaron van den Oord, Yazhe Li, and Oriol Vinyals. Representation learning with contrastive predictive coding. *arXiv preprint arXiv:1807.03748*, 2018.
- [23] Danielle F Pace, Adrian V Dalca, Tal Geva, Andrew J Powell, Mehdi H Moghari, and Polina Golland. Interactive whole-heart segmentation in congenital heart disease. In *Medical Image Computing and Computer-Assisted Intervention–MICCAI 2015: 18th International Conference, Munich, Germany, October 5–9, 2015, Proceedings, Part III 18*, pages 80–88. Springer, 2015.
- [24] Yonglong Tian, Dilip Krishnan, and Phillip Isola. Contrastive multiview coding. In *Computer Vision–ECCV 2020: 16th European Conference, Glasgow, UK, August 23–28, 2020, Proceedings, Part XI 16*, pages 776–794. Springer, 2020.
- [25] Haonan Wang, Peng Cao, Jiaqi Wang, and Osmar R Zaiane. Uctransnet: rethinking the skip connections in u-net from a channel-wise perspective with transformer. In *Proceedings of the AAAI conference on artificial intelligence*, volume 36, pages 2441–2449, 2022.
- [26] Yude Wang, Jie Zhang, Meina Kan, Shiguang Shan, and Xilin Chen. Self-supervised equivariant attention mechanism for weakly supervised semantic segmentation. In *Proceedings of the IEEE/CVF Conference on Computer Vision and Pattern Recognition*, pages 12275–12284, 2020.
- [27] Yawen Wu, Dewen Zeng, Zhepeng Wang, Yiyu Shi, and Jingtong Hu. Distributed contrastive learning for medical image segmentation. *Medical Image Analysis*, 81:102564, 2022.
- [28] Zhirong Wu, Yuanjun Xiong, Stella X Yu, and Dahua Lin. Unsupervised feature learning via non-parametric instance discrimination. In *Proceedings of the IEEE conference on computer vision and pattern recognition*, pages 3733–3742, 2018.

- [29] Xiaowei Xu, Tianchen Wang, Yiyu Shi, Haiyun Yuan, Qianjun Jia, Meiping Huang, and Jian Zhuang. Whole heart and great vessel segmentation in congenital heart disease using deep neural networks and graph matching. In *Medical Image Computing and Computer Assisted Intervention–MICCAI 2019: 22nd International Conference, Shenzhen, China, October 13–17, 2019, Proceedings, Part II 22*, pages 477–485. Springer, 2019.
- [30] Chenyu You, Ruihan Zhao, Lawrence H Staib, and James S Duncan. Momentum contrastive voxel-wise representation learning for semi-supervised volumetric medical image segmentation. In *Medical Image Computing and Computer Assisted Intervention–MICCAI 2022: 25th International Conference, Singapore, September 18–22, 2022, Proceedings, Part IV*, pages 639–652. Springer, 2022.
- [31] Lequan Yu, Shujun Wang, Xiaomeng Li, Chi-Wing Fu, and Pheng-Ann Heng. Uncertainty-aware self-ensembling model for semi-supervised 3d left atrium segmentation. In *Medical Image Computing and Computer Assisted Intervention–MICCAI 2019: 22nd International Conference, Shenzhen, China, October 13–17, 2019, Proceedings, Part II 22*, pages 605–613. Springer, 2019.
- [32] Dwen Zeng, Yawen Wu, Xinrong Hu, Xiaowei Xu, Haiyun Yuan, Meiping Huang, Jian Zhuang, Jingtong Hu, and Yiyu Shi. Positional contrastive learning for volumetric medical image segmentation. In *International Conference on Medical Image Computing and Computer-Assisted Intervention*, pages 221–230. Springer, 2021.
- [33] Pengyue Zhang, Fusheng Wang, and Yefeng Zheng. Self supervised deep representation learning for fine-grained body part recognition. In *2017 IEEE 14th international symposium on biomedical imaging (ISBI 2017)*, pages 578–582. IEEE, 2017.
- [34] Hengshuang Zhao, Jianping Shi, Xiaojuan Qi, Xiaogang Wang, and Jiaya Jia. Pyramid scene parsing network. In *Proceedings of the IEEE conference on computer vision and pattern recognition*, pages 2881–2890, 2017.
- [35] Xiahai Zhuang. Challenges and methodologies of fully automatic whole heart segmentation: a review. *Journal of healthcare engineering*, 4(3):371–407, 2013.
- [36] Xiahai Zhuang and Juan Shen. Multi-scale patch and multi-modality atlases for whole heart segmentation of mri. *Medical image analysis*, 31:77–87, 2016.
- [37] Xinrui Zhuang, Yuexiang Li, Yifan Hu, Kai Ma, Yujiu Yang, and Yefeng Zheng. Self-supervised feature learning for 3d medical images by playing a rubik’s cube. In *Medical Image Computing and Computer Assisted Intervention–MICCAI 2019: 22nd International Conference, Shenzhen, China, October 13–17, 2019, Proceedings, Part IV 22*, pages 420–428. Springer, 2019.

CHD (M=6)	
Number of Blocks	Average Dice
0	0.5243(.05)
1($\lambda = 0.5$)	0.5611(.04)
2($\lambda = 0.25$)	0.5620(.05)
3($\lambda = 0.125$)	0.5543(.05)
4($\lambda = 0.0625$)	0.5560(.05)

Table 5: The ablation studies of number of blocks of the decoder. λ denotes scale factor used in downsampling.

CHD (M=6)		
Backbone	JCL	Random
UNet	0.5620(.05)	0.5198(.06)
AttUNet	0.5772(.04)	0.5493(.06)
UCTransUNet	0.5399(.07)	0.4568(.07)
BCDUNet	0.4427(.08)	0.4068(.05)

Table 6: Comparison results of different variants of UNet backbone.

A Network Architecture

Our proposed JCL framework has three parts: an encoder $e(\cdot)$, a partial decoder $d(\cdot)$ and a projector $g(\cdot)$. The encoder and decoder are based on a UNet architecture and the projector includes an image-level instance projector and a pixel-level pixel projector. Specifically, the encoder $e(\cdot)$ consists of 4 convolutional blocks and a center block. Each convolutional block consists of two "Conv2d \rightarrow BatchNorm2d \rightarrow LeakyReLU" structures followed by a 2×2 Maxpooling layer with stride 2. The kernel size of Conv2d is 3×3 with 1 zero padding. The partial decoder $d(\cdot)$ used in JCL is a two-block part of the whole decoder of UNet which will be used for downstream segmentation tasks. Similar to the encoder, the decoder of UNet also consists of 4 convolutional blocks and a projection head. Each convolutional block consists of a ConvTranspose2d followed by two "Conv2d \rightarrow BatchNorm2d \rightarrow LeakyReLU" structures which is the same as those in the encoder. The projection head is a simple Conv2d structure which will project the fused features into a segmentation map which represents the probability that pixels belong to the background or the K target substructures. As for the partial decoder $d(\cdot)$ in our proposed JCL, it is made up of the first two convolutional blocks from the whole UNet decoder. The projector consists of an image-level instance projector and a pixel-level pixel projector which serves to project the fused features into image-level and pixel-level projections to calculate global contrastive loss \mathcal{L}_g and dense contrastive loss \mathcal{L}_d , respectively. $Z^g \in \mathbb{R}^{B \times C}$ (which B denotes batch size, C denotes channels, 16×128 in our setting) is calculated for image-level global contrastive loss \mathcal{L}_g while $Z^l \in \mathbb{R}^{B \times C \times H \times W}$ (which B denotes batch size, C denotes channels, H denotes image height, W denotes image width, $16 \times 128 \times 32 \times 32$ in our setting) for pixel-level dense contrastive loss \mathcal{L}_d . The image-level instance projector consists of an "AdaptiveAvgPool2d \rightarrow Flatten \rightarrow Linear \rightarrow ReLU \rightarrow Linear" structure while the pixel-level pixel projector consists of a "Conv2d \rightarrow BatchNorm2d \rightarrow LeakyReLU \rightarrow Conv2d \rightarrow BatchNorm2d \rightarrow LeakyReLU" structure. The kernel size of Conv2d is still 3×3 with 1 zero padding.

B Discussion

Different numbers of blocks of decoder: As shown in Table 5, all the frameworks with a decoder outperforms that without a decoder, and the two-block decoder gets the highest dice which is used as a baseline setting for other experiments. Since we need to add downsampling with a scale factor according to the numbers of blocks of the decoder, the input size is perhaps too small when three/four blocks of the decoder, resulting in a damage to image details and thus degrading performance.

Variants U-Net backbones: The decoder used for medical image segmentation are usually U-shape, and our JCL can also be generalized to other variants of U-Net. We have conducted experiments on different variants of U-Net to verify generalization and universality of our proposed JCL. Specifically,

CHD (M=6)		
	Framework	Average Dice
JCL(One Stage)	encoders with EMA	0.5226(.05)
	two independent encoders	0.5126(.06)
	two parameter-shared encoders	0.5620(.05)
JCL(Two Stage)	stage one w downsample	0.5278(.07)
	stage one w/o downsample	0.5341(.06)

Table 7: Comparison results of different connection modes of encoders and different stages of JCL.

Ablation Studies			
Framework	$M = 6$	$M = 10$	$M = 16$
PCL (\mathcal{L}_g)	0.8467(.03)	0.8832(.02)	0.9019(.01)
JCL ($\mathcal{L}_{ER} + \mathcal{L}_g$)	0.8518(.04)	0.8903(.02)	0.9033(.01)
JCL ($\mathcal{L}_{ER} + \mathcal{L}_g + \mathcal{L}_d$)	0.8517(.03)	0.8871(.02)	0.9034(.01)

Table 8: Ablation studies for transfer learning on MMWHS.

we chose UCTransNet (Transformer complement to CNN-based U-Net), Attention U-Net (decoder with attention blocks) and BCDUNet (Bi-directional ConvLSTM U-Net with densely connected convolutions) for comparison with the basic U-Net. The results are shown in Table 6 and we can see that our JCL can be generalized to different model backbones. Specifically, AttUNet even outperforms basic UNet, and UCTransNet obtains an incredible improvement compared with that learning from scratch.

Different forms of pixel-level dense contrastive loss: Before MLC loss of our proposed JCL is fully designed, we conduct a few comparison experiments between different forms of dense contrastive loss \mathcal{L}_d directly plugged into PCL, including MSE loss, BYOL-type loss (which is actually l_2 normalized + MSE used in BYOL) and SupConst loss (which is the form we end up using in our JCL). The results are shown in Table 9. It can be seen that SupConst form \mathcal{L}_d achieves the highest performance with Dice 0.5620 among all kinds of loss forms.

Different connection modes of encoders: Considering there exists different connection modes of encoders in these SOTA methods, such as parameter-shared encoders in SimCLR and SimSiam, and encoder with EMA in MoCo and BYOL. We explore the performance of different connection modes of the encoder between two branches. From Table 7, we can conclude that the parameter-shared mode matters a lot especially in CL with negative sample pairs. Moreover, we further explore the performance between one-stage JCL (pretrain encoder and decoder simultaneously) and two-stage JCL (pretrain encoder and decoder separately). From Table 7, we can see that our JCL in one-stage setting performs much better than JCL in two stage setting (The connection mode of encoders in Stage two of Two-stage JCL is parameter-shared).

Limitation: Our proposed JCL still has some limitations specifically when applied to transfer learning on MMWHS. On the one hand, unfortunately, the performance of our JCL is inferior to PCL when a small number of training samples is used (*e.g.* $M = 2, 4$) from Table 10. On the other hand, the performance of JCL with image-level global contrastive loss \mathcal{L}_g and pixel-level contrastive loss \mathcal{L}_d is inferior to that with only image-level global contrastive loss \mathcal{L}_g according to our ablation studies. The comparison results are shown in Table 8. As far as we are concerned, the reason why the performance of our proposed JCL for transfer learning is relatively unsatisfactory is originated from two parts: (1) Different data distributions between CHD and MMWHS. Although both of them are CT modality datasets with the same seven substructures, however, the data distributions between CHD and MMWHS are inevitably different due to difference of patients, acquisition requirements, etc, which is actually kind of multi-center data. (2) Unique characteristics of pixel-level dense contrastive loss \mathcal{L}_d . Since \mathcal{L}_d concentrates more on local, fine-grained features while \mathcal{L}_g is more focused on global, coarse features of images, the former loss \mathcal{L}_d is certainly more susceptible to pre-trained datasets compared with the latter loss \mathcal{L}_g when transferred to other datasets. To alleviate the above problems, our future work may focus on semi-supervised learning, domain adaption and continue learning, which can unite datasets for both pre-training and fine-tuning in CL settings to achieve higher performance.

Visualization of segmentation results: The visualization results of ablation studies are shown in

CHD (M=6)	
Framework	Average Dice
PCL (no \mathcal{L}_d)	0.5243(.05)
PCL_MSE (MSE form \mathcal{L}_d)	0.5468(.05)
PCL_BYOL (BYOL form \mathcal{L}_d)	0.5164(.06)
PCL_SupConst (SupConst form \mathcal{L}_d)	0.5500(.05)
JCL (Multi-level contrastive loss \mathcal{L}_{MLC})	0.5620(.05)

Table 9: Comparison results of different forms of pixel-level dense contrastive loss on CHD with M=6.

CHD transferring to MMWHS		
Method	$M = 2$	$M = 4$
PCL	0.5316(.18)	0.8001(.05)
JCL	0.5004(.21)	0.7983(.06)

Table 10: Comparison results and ablation studies for transfer learning on MMWHS.

Figure 5. We can also tell the contribution from each part of our proposed components: *i.e.* we can get a tremendous promotion with 5.5% mIoU under the introduction of decoder structure, and 1.2% and 0.98% mIoU promotion under the introduction of \mathcal{L}_{ER} and \mathcal{L}_d , respectively when $M = 10$ of CHD.

The visualization of more segmentation results of our JCL, the previous best methods PCL and GCL, and the baseline CL methods on MMWHS, CHD and HVSMR is shown in Figure 4. The visualization results of more ablation studies are shown in Figure 6.

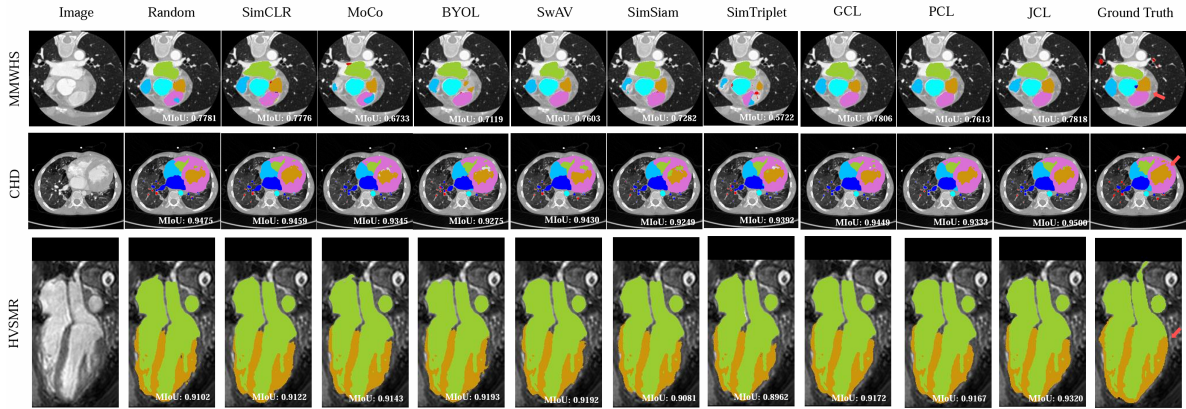


Figure 4: Visualization of segmentation results on all datasets. The results of MMWHS, CHD, and HVSMR are generated from the fine-tuned models of $\{M=6, \text{fold}=0\}$, $\{M=15, \text{fold}=3\}$ and $\{M=2, \text{fold}=4\}$, respectively. M is the number of patients used for fine-tuning.

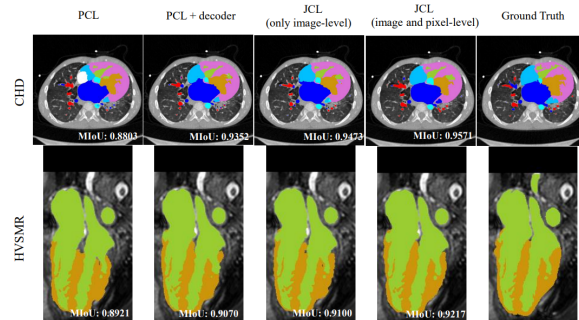


Figure 5: Visualization of segmentation results on CHD and HVSMR for ablation studies. The results of CHD and HVSMR are generated from the fine-tuned models of $\{M=10, \text{fold}=3\}$ and $\{M=2, \text{fold}=4\}$. M is the number of patients used for fine-tuning.

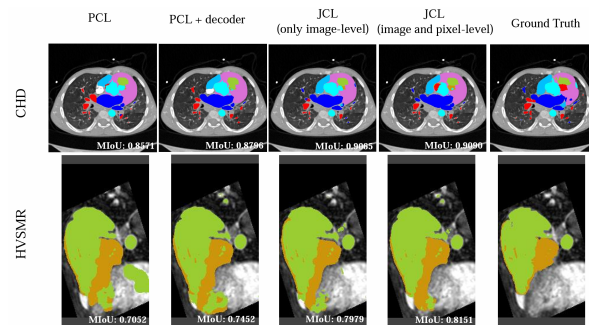


Figure 6: Visualization of segmentation results on CHD and HVSMR for ablation studies. The results of CHD and HVSMR are generated from the fine-tuned models of $\{M=15, \text{fold}=3\}$ and $\{M=2, \text{fold}=3\}$. M is the number of patients used for fine-tuning.